



DIGITAL ACCESS TO SCHOLARSHIP AT HARVARD

Regional CO Pollution in China Simulated by the High-Resolution Nested-Grid GEOS-Chem Model

The Harvard community has made this article openly available.
[Please share](#) how this access benefits you. Your story matters.

Citation	Chen, Dan, Yuxuan Wang, Michael B. McElroy, Kebin He, Robert M. Yantosca, and Philippe Le Sager. 2009. Regional CO pollution in China simulated by the high-resolution nested-grid GEOS-Chem model. Atmospheric Chemistry and Physics Discussions 9: 5853-5887.
Published Version	http://www.atmos-chem-phys-discuss.net/9/5853/2009/
Accessed	February 18, 2015 3:58:23 AM EST
Citable Link	http://nrs.harvard.edu/urn-3:HUL.InstRepos:5029363
Terms of Use	This article was downloaded from Harvard University's DASH repository, and is made available under the terms and conditions applicable to Open Access Policy Articles, as set forth at http://nrs.harvard.edu/urn-3:HUL.InstRepos:dash.current.terms-of-use#OAP

(Article begins on next page)

Regional CO pollution in China simulated by the high-resolution nested-grid GEOS-Chem model

Dan Chen¹, Yuxuan Wang^{1,2,*}, Michael B. McElroy², Kebin He^{1,*}, Robert M. Yantosca², Philippe Le Sager²

¹ Department of Environmental Science and Engineering, Tsinghua University, Beijing, China

² Division of Engineering and Applied Sciences and Department of Earth and Planetary Sciences, Harvard University, Cambridge, Massachusetts, USA

Manuscript submitted to Atmospheric Chemistry and Physics Discussions

January 20, 2009

Do not quote, cite, or copy

* Correspondence to Y. Wang (yxw@tsinghua.edu.cn) or K. He (hekb@tsinghua.edu.cn)

1 **Abstract**

2 An updated version of the nested-grid GEOS-Chem model is developed allowing for higher
3 horizontal ($0.5^\circ \times 0.667^\circ$) and vertical resolution as compared to global models. CO transport
4 over a heavily polluted region, the Beijing-Tianjin-Hebei (BTH) city cluster in China, and the
5 pattern of outflow from East China in summertime are investigated. Comparison of the
6 nested-grid with global models indicates that the fine-resolution nested-grid model is capable of
7 resolving individual cities with high associated emission intensities. The nested-grid model
8 indicates the presence of a high CO column density over the Sichuan Basin in summer,
9 attributable to the low-level stationary vortex associated with the Basin's topographical features.
10 The nested-grid model provides good agreement also with measurements from a suburban
11 monitoring site in Beijing during summer 2005. Tagged CO simulation results suggest that
12 regional emissions make significant contributions to elevated CO levels over Beijing on polluted
13 days and that the southeastward moving cyclones bringing northwest winds to Beijing are the key
14 meteorological mechanisms responsible for dispersion of pollution over Beijing in summer.
15 Overall CO fluxes to the NW Pacific from Asia are found to decrease by a factor of 3-4 from
16 spring to summer. Much of the seasonal change is driven by decreasing fluxes from India and
17 Southeast Asia in summer, while fluxes from East China are only 30% lower in summer than in
18 spring. Compared to spring, summertime outflow from Chinese source regions is strongest at
19 higher latitudes (north of 35° N). The deeper convection in summer transporting CO to higher
20 altitudes where export is more efficient is largely responsible for enhanced export in summer.

21 **Keywords:** nested-grid, model resolution, China, CO, summer outflow

22 1 Introduction

23 Chemical transport models are effective in simulating the combined influences physical and
24 chemical processes affecting the distribution of a key chemical species in the Earth's atmosphere.
25 The domain of an atmospheric model varies from hundreds of meters to thousands of kilometers
26 (Seinfeld and Pandis, 1998). Global climate change or stratospheric ozone depletion is simulated
27 over a global scale domain and over periods ranging from months to hundreds of years and
28 beyond. Specific air pollution issues such as acid deposition and long-range transport of
29 particulates and ozone are simulated over synoptic to global-scale domains over periods of days
30 to months. Urban air pollution is simulated over micro- to mesoscale domains over periods
31 ranging from hours to days. It's difficult to simulate the variation of species concentrations at
32 scales smaller than the model resolution. For example, a global scale model that treats the entire
33 area as one computational cell of uniform chemical composition cannot describe the spatial
34 variations in pollution levels across the two adjacent large Chinese cities of Beijing and Tianjin .

35 The diffusion equation in regional atmospheric models needs side boundary conditions in
36 the x, y, and z directions, whereas global models simulate the Earth's atmosphere as a whole. It is
37 difficult to obtain exact values of tracer concentrations for all points of the side boundaries as a
38 function of time. Boundary conditions, especially at the upwind boundaries, continue to affect
39 model predictions throughout the simulation. Song et al. (2008) used the simulation results of a
40 global chemistry model, the Real-time Air Quality Modeling System (RAQMS), to provide
41 dynamic lateral boundary conditions for regional air quality simulations using the Models-3

42 Community Multiscale Air Quality (CMAQ) Model. They found that use of the dynamic
43 boundary conditions not only improved CMAQ's simulations of diurnal variations resolving the
44 daily maxima of surface O₃ but resulted also in better agreement with the vertical structure of O₃
45 measured in the middle and upper troposphere. Compared to the simulation with predefined
46 lateral boundary condition profiles, it is suggested that at the upper troposphere more than 85%
47 of the O₃ concentration difference associated with the lateral BCs was caused by the transport
48 and diffusion processes . The regional and global models employed in their study, however, used
49 different meteorological fields, employed different chemical mechanisms, and also differed in
50 their treatments of transport. Wang et al. (2004a) developed a one-way nested-grid capability in
51 the global GEOS-Chem model based on GEOS-3 meteorology. The nested-grid formulation
52 included a regional window with relatively high spatial resolution (1° (latitude) x 1° (longitude))
53 imbedded in a lower-resolution global context (4° x 5°) of the GEOS-Chem model. Results from
54 the coarse global model simulation were used to drive the nested-grid model through
55 time-varying boundary conditions. The high-resolution, nested-grid simulation employed the
56 same meteorology, dynamics, and chemistry as the global GEOS-Chem model. Through detailed
57 analysis of improvements in CO simulations that were simply the consequences of increasing the
58 spatial resolutions, Wang et al. (2004a) found that the higher-resolution model allowed for more
59 efficient, advection-related ventilation of the lower atmosphere, reflecting the significance of
60 localized regions of intense upward motion not resolved in the coarser-resolution simulation. The
61 nested-grid GEOS-Chem model has been employed in a variety of applications for East Asia
62 (Wang et al., 2004a, 2004b), North America (Fiore et al., 2006; Li et al., 2006; Park et al., 2006),

63 and Europe. However, even the higher resolution of $1^\circ \times 1^\circ$ is still too coarse to address concerns
64 relating to regional-scale air quality over complex terrains or in regions characterized by complex
65 patterns of emissions.

66 This work follows the methodology of Wang et al. (2004a) to develop an updated version of
67 the nested-grid capability in the global GEOS-Chem model (Bey et al., 2001) using the newest
68 version of GEOS-assimilated meteorological data (GEOS-5), which allows for higher spatial
69 resolutions over the nested domain. Compared to the original version of the nested-grid
70 GEOS-Chem model designed for GEOS-3 meteorology with a horizontal resolution of $1^\circ \times 1^\circ$
71 and 10 sigma levels below 2 km, the GEOS-5 meteorology allows for spatial resolutions of $0.5^\circ \times$
72 0.667° with 15 hybrid eta levels below 2 km for the nested domain. The horizontal and vertical
73 resolution of the GEOS-5 nested-grid model is comparable to that of many regional-scale models.
74 For purpose of this application the nested domain with high resolution ($0.5^\circ \times 0.667^\circ$) is set over
75 East Asia, where rapid economic growth in recent years has resulted in large increases in
76 pollutant emissions with implications for the global environment. The nested-grid capability can
77 be easily adopted for other regions of the globe (Fiore et al., 2005; Li et al., 2005).

78 This work focuses on summertime transport of pollutants over a particular region of China,
79 the Beijing-Tianjin-Hebei (BTH) city cluster. Consisting of only 2.3% of China's land area, the
80 BTH city cluster accounts for 10.5% of China's SO_2 emissions and 10.9% of its NO_x emissions
81 (Zhang et al., 2009). Taking advantage of the increased horizontal resolution of $0.5^\circ \times 0.667^\circ$
82 (roughly 40km x 50km over China), it is possible for the nested-grid GEOS-Chem model to

83 resolve the heterogeneous transport and emission patterns over the BTH city cluster. CO is used
84 as a convenient tracer to indicate the frequency and magnitude of influences from vehicle
85 emissions and other combustion sources related to urban pollution. Many previous studies have
86 examined the mechanisms controlling the outflow of CO from Asia to the NW Pacific in
87 springtime, the season with maximum export fluxes (Liu et al., 2003; Fuelberg et al., 2003; Liang
88 et al., 2004). Little attention has been paid to pollution and outflow from China in summertime.
89 The present study will examine the outflow pattern and efficiencies for export of CO from China,
90 focusing on differences between spring and summer.

91 The nested-grid approach adopted here is described in Section 2. The high-resolution
92 nested-grid simulation is evaluated in Section 3 comparing the present results with surface
93 observations and with results from the coarse resolution model. The nested-grid model is
94 employed in Section 4 to examine the meteorological conditions regulating day-to-day variations
95 in CO at a suburban site in Beijing. Tagged CO simulations were conducted to estimate the
96 contributions of local and regional emissions to CO levels over Beijing. In Section 5, we compare
97 the outflow pattern and export efficiencies of CO from China between spring and summer.
98 Concluding remarks are presented in Section 6.

99 **2 Model Approach**

100 The GEOS-Chem global 3-D model for tropospheric chemistry is driven by meteorological
101 data assimilated by the Goddard Earth Observing System (GEOS) at the NASA Global Modeling
102 and Assimilation Office (GMAO) (Bey et al., 2001). The GEOS assimilated meteorology has

103 gone through many versions over the past ten years, evolving from GEOS-1 to the most recent
104 version of GEOS-5. The present study used GEOS-5 meteorology extending from Dec 2004 to
105 present. We chose in this application to use GEOS-Chem version 8-01-01
106 (<http://www.as.harvard.edu/chemistry/trop/geos>), the first version of GEOS-Chem that is fully
107 compatible with the GMAO GEOS-5 operational meteorology data. Meteorology fields in the
108 GEOS-5 data have a temporal resolution of 6 hours (3 hours for surface variables and mixing
109 depths) and a horizontal resolution of 0.5° latitude by 0.667° longitude, with 72 hybrid eta levels
110 in the vertical column that extending from the surface to 0.01 hPa. The lowest 2 km is resolved
111 by 14 layers with midpoints at altitudes of 70, 200, 330, 470, 600, 740, 880, 1000, 1160, 1300,
112 1440, 1600, 2000 m for a column based at sea level. Details of this data source are presented
113 elsewhere (Rienecker et al., 2007). For inputs to the global GEOS-Chem model, the horizontal
114 resolution of the meteorological fields is degraded to 2° x 2.5° longitude or 4° latitude x 5°
115 longitude due to computational limitations. Details of the degradation process are provided by
116 Wang et al. (2004a). Compared to the global GEOS-Chem model, the nested-grid GEOS-Chem
117 model retains a generic high horizontal resolution over the nested regional domain.

118 The GEOS-5 meteorology uses an advection code different from that of GEOS-3, partly
119 because different vertical coordinates were used in the two versions of GEOS assimilated
120 meteorology. Lateral boundary conditions for the nested-grid model were added in the GEOS-5
121 advection code following the same methodology of Wang et al. (2004a). The nested regional
122 domain (70°E–150°E, 11°S–55°N; c.f. Fig. 1 in Wang et al., 2004a) includes all of China, its

123 neighboring countries (stretching from Pakistan in the west to Japan in the east and from
124 Indonesia in the south to Mongolia in the north), and a significant portion of the northwestern
125 Pacific. The high resolution regional domain is nested into a global domain treated with a
126 resolution of $4^\circ \times 5^\circ$. The outermost grids at the lateral boundaries of the high-resolution
127 nested-grid domain were used to delineate a buffer zone separating low and high-resolution
128 portions of the model (Wang et al., 2004a). To provide boundary conditions for the regional
129 model, the global assimilation was run at the spatial resolution of 4 degrees latitude by 5 degrees
130 longitude. The tracer mixing ratios for the buffer zone grids were saved for every three hours
131 consistent with the temporal resolution of the meteorology data. The archived, time-varying
132 boundary conditions were used to drive high-resolution nested-grid model runs.

133 **3 CO Simulations with different resolutions**

134 A CO-only simulation was conducted using the global model with its higher resolution
135 nested-grid for summer 2005 with specified OH fields derived from a global coupled
136 NO_x -VOCs- O_3 -aerosol simulation (Wang et al., 2004a). The global simulation was conducted
137 first at $4^\circ \times 5^\circ$ resolution (referred to as the coarse-resolution global model) and then at $2^\circ \times 2.5^\circ$
138 resolution (referred to as the intermediate-resolution global model). To avoid transients
139 associated with initial conditions, the coarse-resolution global model was run for one month
140 beginning on 1 December 2004. Results for 1 January 2005 were saved and interpolated onto the
141 $2^\circ \times 2.5^\circ$ and $0.5^\circ \times 0.667^\circ$ grids providing initial conditions for the intermediate global model
142 and the associated high-resolution nested-grid. Simulations with different resolutions were

143 conducted for the period from Jan to Sep 2005. Boundary conditions for the nested-grid model
144 were provided by the coarse-resolution global model (i.e., 4° X 5° resolution). Results were
145 presented for Jul to Sep 2005, allowing sufficient time for the high-resolution model to adjust to
146 transients introduced by the initialization of the model on 1 January 2005.

147 In this section, we examine the differences relating to the higher spatial resolution available
148 in the nested-grid regional domain by comparing high-resolution nested-grid model outputs with
149 the intermediate-resolution global simulation. Since the simulations with different resolutions
150 adopted the same OH fields, differences in modeling CO may be entirely attributed to the higher
151 resolution specification of sources and to differences in the treatment of transport as simulated
152 using the one-way nested formulation.

153 **3.1 CO Emissions**

154 Anthropogenic emissions of CO from the combustion of fossil fuel and biofuel over the
155 nested East Asia domain were taken from Zhang et al. (2009) for the year 2006. For China, the
156 inventory was based upon the studies of Streets et al. (2006), which improved estimations for
157 emissions from Chinese industrial sources that had been underestimated in the inventory
158 developed earlier in support of the TRACE-P aircraft mission (Streets et al., 2003). The updated
159 inventory was downloaded from <http://mic.greenresource.cn/intex-b2006> at 0.5° X 0.5°
160 resolution. The 0.5°x0.5° gridded emission inventory was degraded into 4°x5°, 2°x2.5°,
161 0.5°x0.667° using spatial averaging.

162 For emissions associated with fossil fuels over the rest of the world, we adopted inventories

163 reported by Duncan et al. (2003). Emissions due to the combustion of biofuel and the burning of
164 biomass were taken from Yevich and Logan (2003) and Duncan et al. (2003), respectively. These
165 emissions were defined with respect to a 1° X 1° grid. The 1° X 1° emissions data sets were
166 regridded to match the 4° X 5°, 2° X 2.5°, 0.5° X 0.667° model resolutions.

167 The spatial distribution of composite CO emissions over the nested domain is presented in
168 Fig. 1a. The emission distribution in China shows the characteristics of the fossil fuel and biofuel
169 combustions spatially differentiated by economic development, industry structure, and population.
170 At 0.5° x0.667° resolution, the inventory explicitly resolves contributions from several Chinese
171 urban regions with high emission intensities (Zhang et al., 2009): a) cities with higher levels of
172 urbanization and motorization, such as Beijing (116.46° E, 39.92° N), Shanghai (121.48° E,
173 31.22° N), and Guangzhou (113.23° E, 23.16° N), where the transportation sector contributes
174 40-60% of CO emissions, b) cities such as Anshan (123.00° E, 41.8° N), Shijiazhuang (114.48
175 ° E, 38.03° N), and Taiyuan (112.53° E, 37.87° N), with heavy industrial manufacturing
176 where industrial sources contribute more than 40% of total emissions, and c) densely populated
177 such as Chongqing (106.54° E, 29.59° N), Tianjin (117.2° E, 39.1° N), and Wuhan (114.31°
178 E, 30.52° N), cities with multiple sources. Most of these cities can be identified in Fig. 1a as
179 individual “hot” spots, while Beijing, Tianjin, and Shijiazhuang are located so close together as to
180 merge into one, large region with high emissions.

181 The ability of the high-resolution nested-grid model to resolve the heterogeneity of
182 emissions over the Beijing-Tianjin-Hebei (BTH) city cluster is illustrated in Fig. 1b. For

183 comparison, Fig. 1c shows emissions for the same region at $2^\circ \times 2.5^\circ$ resolution. The emission
184 data at $0.5^\circ \times 0.667^\circ$ resolution resolve the differences in emission intensities in individual cities,
185 whereas Beijing, Tianjin, and a part of Hebei province are aggregated in the $2^\circ \times 2.5^\circ$ description.
186 The increase of model resolutions from $2^\circ \times 2.5^\circ$ to $0.5^\circ \times 0.667^\circ$ enhanced the ability of the
187 model to represent emissions at the scale of individual cities, although the $0.5^\circ \times 0.667^\circ$
188 resolution is still not fine enough to capture spatial variations in emissions within a particular
189 city.

190 **3.2 CO Mixing ratios**

191 Spatial distributions of CO mixing ratios (ppb) for Aug 2005 averaged over the whole
192 tropospheric column are presented in Fig. 2a-b. The figure includes results from the
193 high-resolution nested-grid model (Fig. 2a) and the intermediate-resolution global model (Fig.
194 2b). Results from the coarse-resolution global model are similar to those from the
195 intermediate-resolution model and are not included. Spatial patterns are similar for the two
196 models, with high mixing ratios in regions of high anthropogenic emissions, notably central and
197 eastern China. It is interesting to note that the mean column mixing ratio of CO displays a
198 distinct peak over the Sichuan Basin (the black squares in Fig. 2) in the high-resolution
199 nested-grid model, but the peak is not so obvious in the intermediate global model. Under the
200 influence of the southwest East Asian summer monsoon, the special topography of the Tibetan
201 Plateau to the northwest makes the Sichuan Basin a favorable location for stationary low-level
202 vortices, or the so-called the southwest vortex (Chang et al., 2002), which tend to trap pollutants

203 within the columns above the Basin. The resolution of the intermediate global model is too coarse
204 to resolve the terrain effects of the Basin and the meteorological features accordingly.

205 Spatial distributions of surface CO mixing ratios are presented in Fig. 2c-d. Spatial patterns
206 are similar for the two models, reflecting emission characteristics with the highest concentrations
207 in Kalimantan Island, South Asia, notable for its regions of high biomass burning. High mixing
208 ratios of CO are found for the Beijing-Tianjin-Hebei region, central and eastern China, and the
209 Sichuan Basin. At $0.5^\circ \times 0.667^\circ$ resolution, the individual grids with high mixing ratios (Fig. 2c)
210 can be easily mapped to the locations of the cities with high emissions as indicated in Fig. 1b,
211 illustrating a clear contrast with surrounding grids that have relatively low CO. At $2^\circ \times 2.5^\circ$
212 resolution, however, emissions from these cities are smeared out to a larger area, resulting in
213 lower concentrations in cities, compensated by higher concentrations in surrounding grids.

214 **3.3 Differences between urban and suburban grids**

215 We examine in this section the extent to which the nested-grid model with its current
216 $0.5^\circ \times 0.667^\circ$ resolution can differentiate between urban and suburban areas with different
217 emission intensities. The intermediate global model is used for comparison. We focus on the
218 BTH city cluster, one of the most populous and polluted regions in China. The surface CO
219 mixing ratio simulated by the nested-grid model and the intermediate global model for this region
220 is displayed in detail in Fig. 3a and 3b, respectively. Two adjacent grids over Beijing with
221 available CO observations, an urban grid (center 116.67° E, 40.00° N) and a suburban grid
222 (Dingling, DL for short, grid center 116.00° E, 40.00° N), were chosen for comparison. Their

223 locations are shown in Fig. 3c. Within the urban grid, there are six monitoring sites covering
224 commercial, residential, and transportation environments. The suburban grid has only one surface
225 station, DL (116.2° E, 40.22° N), located 42 km northwest of Beijing's urban center. Hourly
226 observations of CO mixing ratios at the seven sites within the two grids were collected by the
227 Beijing Municipal Environmental Monitoring Center.

228 Beijing is situated at the northern tip of the roughly triangular North China Plain with a
229 northwest high and a southeast low as its primary topographical features. The northern part is
230 dominated by the Yanshan and Taihang Mountains, which intersect and form a semicircle called
231 the "Beijing Bend." Another large city, Tianjin Municipality (population of about 10 million) is
232 located 150 km southeast of Beijing. The terrain around Tianjin is generally flat and swampy near
233 the coast and hilly in the far north. The climate of the BTH region in summertime is influenced
234 by the East Asian summer monsoon with prevailing southwest winds at the surface.

235 The monthly mean mixing ratios of CO during three months (July, August, and September)
236 in 2005 are summarized in Table 1, including both observations and model results for comparison.
237 The data are represented as daily (24hr) and daytime (10:00-18:00) averages. The monthly mean
238 (both daily and daytime means) mixing ratios of CO as simulated by the 0.5° x 0.667°
239 nested-grid model for both the urban grid and suburban grid are higher than the values derived
240 using the intermediate global model and in better agreement with the observations. Due to
241 resolution limitations, the urban grid in the intermediate global model (2°x2.5° resolution)
242 includes not only the Beijing area, but also Tianjian and a great part of Hebei province, while the

243 suburban grid includes a large part of rural Beijing and Hebei. Here we compare the
244 grid-averaged model results with point observations close to high emission areas (i.e., Beijing),
245 where the smaller the model grid, the less diluted the emissions from Beijing and thus the higher
246 the CO concentrations predicted by the model. The table clearly attests to the improvement in the
247 simulation obtained by increasing the model resolution from $2^\circ \times 2.5^\circ$ to $0.5^\circ \times 0.667^\circ$, as
248 indicated by comparison of results in Fig. 3a and 3b.

249 Compared with the observation, concentrations derived using the $0.5^\circ \times 0.667^\circ$ model are still
250 too low for both the urban and the suburban DL grids. The modeled mixing ratios at the urban
251 Beijing grid and the suburban DL grid are 39% and 11% lower than the observations. The
252 underestimates of daily mean mixing ratios by the model may be partly due to underestimates of
253 CO emissions as inventory estimates for Chinese CO emissions are still uncertain (Zhang et al.,
254 2009). More importantly, the six monitoring sites within the urban grid are all located within a 10
255 km range of the city center, while the urban emissions as simulated in the nested-grid model,
256 even given its relative high applied resolution ($0.5^\circ \times 0.667^\circ$) are much more diluted.

257 **4 A Case Study: Summertime CO variations in Beijing**

258 To investigate the meteorological factors responsible for the alternations between heavy
259 pollution days and clean days in the BTH region in summertime, we first compared the modeled
260 and observed time series of CO mixing ratios and related meteorological parameters for Jul 2005
261 at the DL site. The reason for focusing on the suburban DL site rather than on the urban site is
262 because the resolution limitation of the nested-grid model made it impossible to simulate the very

263 high CO levels at the urban site as indicated above.

264 **4.1 Day-to-day variations in CO and meteorology**

265 Time series of CO daily mixing ratios observed at the urban site and the suburban DL site
266 are summarized in Fig. 4a. As discussed, the DL site was readily impacted by plumes with high
267 levels of CO from the urban grid during the daytime, resulting in high temporal correlations
268 between CO observations at the two sites ($r = 0.82$). Given the nested-grid model resolution, it
269 was difficult for the model to simulate the exact timing and locations of the urban plume.
270 Therefore, when we compared the daily CO levels between modeled results and observations at
271 the DL site, we excluded the impact of urban plumes by filtering out the observations with
272 hourly-mean CO mixing ratios greater than 1300 ppbv. The daily mean CO mixing ratios from
273 the model were based on hourly model outputs sampled in the same way as with the observations.
274 The filtered time series of observed and predicted CO daily concentrations at the DL sites are
275 presented in Fig. 4b. After excluding the impact of urban plumes with very high CO mixing
276 ratios, the modeled CO at the DL site showed overall good agreement with the observations in
277 terms of temporal variability. Modeled values are lower than the observations in general, which is
278 often the case when point measurements are compared with grid-averaged model predictions.
279 Other possible explanations for the low bias of the model results include uncertainties in CO
280 emissions (both in magnitude and spatial distribution) and the model's overestimate of wind
281 speeds as discussed below.

282 The comparisons of temperature and surface pressure between the model and observations

283 are presented in Fig. 4c. The model reproduces the day-to-day variations in temperature and
284 surface pressure. The correlation coefficients between model and observations are 0.87 for
285 temperature and 0.98 for surface pressure. Figure 4d compare model and observed values of daily
286 wind speed at the surface. The correlation coefficient for wind speed was 0.62 for the whole
287 month, with the model tending to overestimate wind speeds for most days. There were some
288 cases where the model did a satisfactory job in simulating variations in both CO and wind speeds.
289 For example, the relatively high mixing ratios of CO observed on 2 and 3 July were associated
290 with relatively low wind speeds. The model reproduced the variability in CO and winds during
291 these two days. The period of 25 and 26 July saw another successful simulation of CO and wind
292 speeds by the model. But during 18 – 20 July, for example, the model overestimated wind speeds
293 and underestimated CO mixing ratios to a large degree. Depending on local wind directions, the
294 DL site may be influenced directly by urban emissions from Beijing or by regional pollution. If
295 the DL site is under the strong influence of Beijing urban emissions, overestimates in wind
296 speeds by the model may result in more rapid dilution and greater export of local emissions out
297 of the grid, leading to the model's underestimates of CO mixing ratios at DL.

298 **4.2 Regional versus local influences**

299 To quantify the effects of different source regions on pollution levels over Beijing in
300 summertime, we conducted a tagged CO simulation in which anthropogenic emissions of CO
301 from the following seven Chinese regions were labeled and independently transported in the
302 model: NEC (Northern East China), BJ (Beijing, consisting of only the urban grid and the

303 suburban DL grid), TH (Tianjin-Hebei), SH (Shandong and parts of Hebei.), SX (Shanxi and
304 Shaanxi.), SC (South China), and West China. In addition, emissions from India and South Asia
305 were also tagged as they make important contributions to Asian outflow of CO to the NW Pacific
306 as discussed in the next section. The tagged regions of emissions are indicated in Fig. 5. Detailed
307 methodology of the tagged CO simulation was described in Wang et al. (2004a).

308 Table 2 summarizes the percentage contributions of individual CO tracers to total CO
309 simulated at the DL site for each month. Emissions from the two Beijing grids (i.e., the urban
310 grid and the suburban DL grid, denoted as BJ in the table) were referred to as local emissions in
311 our study, while emissions from all the other tagged Chinese regions were regarded as regional
312 emissions. We found that local emissions make up an average about 46% of CO mixing ratios at
313 the DL site in summer. The regional emissions from the tagged Tianjin-Hebei region make up the
314 second largest contribution, accounting for an average of 17% for CO at DL. The temporal
315 correlation between the tagged BJ tracer (representing local emissions) and the TH tracer is 0.52.
316 The tagged SH tracer was also found to correlate well with the BJ tracer, although the
317 contribution from the SH tracer is much smaller.

318 For air quality regulators, an important question is how to reduce pollutant concentrations on
319 days with bad air quality. On those days, the relative contributions from local and regional
320 emissions may differ from their mean contributions. Therefore, we now turn our attention to the
321 contributions of tagged tracers on individual days. Figure 6 presents the day-to-day variations in
322 mixing ratios of individual tagged tracers for July 2005. Most days, the BJ tracer makes the

323 biggest contribution , but its relative importance becomes smaller on high pollution days with
324 high mixing ratios of CO. For example, during the high pollution period between 6 July and 8
325 July, the BJ tracer accounted for only 35%-40% of the total CO, while the influence from
326 regional emissions was much higher, with the TH tracer and the SH tracer accounting for about
327 35% and 20%, respectively, during the period. On relatively clean days (5 Jul and 28-29 Jul), the
328 BJ tracer (70-75%) and the global background made the biggest contributions. The tagged CO
329 simulation indicates that during periods of heavy pollution the Beijing, Tianjin-Hebei, Shandong,
330 and Hebei regions were particularly important source regions.

331 **4.3 Meteorological Conditions**

332 To investigate the meteorological conditions controlling the differences between heavily
333 polluted and relatively clean days in summer, we chose 1-4 July as a representative period. The
334 mixing ratios of CO observed at the DL site were relatively low on 1 July, rose to a high level on
335 the second day and peaked on 3 July, followed by a rapid drop on 4 July. During this period of 4
336 days, the observed variations in CO mixing ratios differed by about a factor of three. The model
337 reproduced well the sequence of variations, although it failed to reproduce the exact magnitude of
338 the very high and very low mixing ratios of CO on 3 July and 4 July, respectively.

339 Fig. 7 displays the distribution of winds and CO mixing ratios in the boundary layer as
340 simulated by the model for each of the four days. From 2 Jul to 4 Jul, under the high pressure
341 system over the East China Sea (the Pacific High), surface wind patterns indicate a strong
342 maritime influence from southeast and central China with a general southeast onshore flow along

343 the coast. On Jul 2, a weak low-pressure system was centered over Mongolia, northwest of
344 Beijing. The Beijing area was not strongly influenced by either the low-pressure system to the
345 northwest or the high-pressure system to the southeast. A weak high-pressure system was located
346 over the North China Plain, and the atmosphere was relatively static over Beijing on 3 July, with
347 surface wind speeds below 1 m/s. The static conditions favored accumulation of the regional CO
348 emissions from the heavily polluted Tianjin-Hebei area and local Beijing emissions, resulting in
349 rapid rises in CO mixing ratios. The low-pressure system strengthened on 3 and 4 July and
350 moved toward the southeast. By 4 July, the low-pressure center was to the east of Beijing, with
351 the associated strong northwesterly winds bringing relatively clean air to Beijing with CO levels
352 over Beijing dropping accordingly. The meteorological setting for Jul 2 to 4 is consistent with the
353 general description of the sawtooth cycles of PM_{2.5} levels over Beijing, as reported by Jia et al.
354 (2008). They suggested that the passage of synoptic systems from the north is the key
355 meteorological mechanism resulting in the dilution and removal of pollution from Beijing.

356 **5 China Outflow**

357 The monsoonal circulation over East Asia is characterized by a general outflow of surface
358 air from the continent in winter compensated by a maritime inflow in summer. Many previous
359 studies have used CO as a tracer to examine the patterns and mechanisms of Asian outflow to the
360 Pacific, and much of the attention has thus far been paid to springtime (Liu et al., 2003; Fuelburg
361 et al., 2003; Liang et al., 2004). Liu et al. (2003) found that the major process responsible for the
362 export of Asian anthropogenic pollution to the western Pacific during spring is frontal lifting to

363 the free troposphere (FT) ahead of southeastward-moving cold fronts and transport in the
364 boundary layer (BL) behind the cold front. Orographic lifting over central and eastern China
365 combines with the cold fronts to promote the transport of Chinese pollution to the FT. In this
366 section, the outflow pattern in summertime is discussed and compared with that in spring. The
367 analysis focuses on CO emitted from the geographical regions in Asia as defined in the tagged
368 CO simulation described above (c.f. Fig. 5). The domain adopted to evaluate the export fluxes is
369 defined by 80°-140°E longitude, 10°-50°N latitude, and 0-12 km altitude. The regions of SH, TH,
370 and BJ are combined here into the North China (NC) region.

371 Figure 8 presents the monthly (Mar – Sep 2005) mean fluxes of CO through the eastern
372 (140°E) boundary. The CO fluxes displayed in the figure are partitioned among three source
373 regions, namely India, Southeast Asia, and East China (the aggregation of NC, SC, NEC, and
374 SX). The geographical definition of these regions is shown in Fig. 5. The fluxes through the
375 eastern boundary are positive (eastward) for each month. The overall fluxes in springtime are
376 larger by a factor of 2-3 than the fluxes in summertime, consistent with the seasonality suggested
377 by Liu et al. (2003) for the export of Asian anthropogenic CO to the NW Pacific. CO originating
378 from India and Southeast Asia accounts for about 60% of the total fluxes in spring. The fraction
379 from these sources drops to 30% in summer. Seasonal biomass burning over India and Southeast
380 Asia is responsible for the large export of CO from the two regions in spring. The seasonal
381 variability in outflow from East China is relatively small, with summertime outflow only 30%
382 lower than that in springtime. Emissions of CO from East China are responsible for about 40% of

383 the total outflow of CO from Asia in spring, with the fraction increasing to 70%-80% in summer.

384 Table 3 summarizes the export efficiency of CO emitted from the tagged source regions in
385 springtime (MAM) and summertime (JJA). The export efficiency of CO, evaluated separately for
386 the north-south (northward as positive) and east-west (eastward as positive) directions, is defined
387 as the ratio of the net export through the lateral boundaries to the total emissions from the source
388 region. From the table, we can see that in both seasons the major export pathway is in the EW
389 direction for all source regions. It has been suggested in many previous studies that CO emitted
390 over Asia is transferred eastward through a two-step process (Liu et al., 2003; Wang et al., 2004;
391 Fuelburg et al., 2003; Liang et al., 2004). First, it is lifted through vertical motions of the
392 atmosphere (e.g, by fronts or convection) from the near-surface regions to higher altitudes.
393 Subsequently, it is captured by strong westerlies that prevail in the free troposphere. Among the
394 regions listed in Table 3, SC has the highest EW export efficiency because its location in the
395 lower latitude with abundant solar radiation is conducive to stronger vertical motions of the lower
396 atmosphere, resulting in efficient lifting of CO to the free troposphere. NEC has the highest NS
397 export efficiency because of its location near the northern boundary. The EW export efficiency is
398 higher in summer and so is the efficiency for NS export. The total export efficiency ranges from
399 0.45 (NC) to 0.65 (SC) in spring and from 0.66 (NC) to 0.89 (SX) in summer. The deeper
400 convection in summer bringing CO to higher altitudes with more efficient export is the important
401 factor for higher export efficiency in summer.

402 Figure 9 presents latitude-altitude cross sections at 140°E of seasonal mean fluxes from the

403 tagged East China regions for spring (MAM) (upper panels) and summer (JJA) (lower panels) 2005.
404 Compared with springtime, summertime outflow from all the tagged Chinese source regions is
405 strongest at higher latitudes (north of 35°N). Inflow (i.e., negative fluxes) prevails through the whole
406 troposphere south of 25°N in summer. This suggests that in summer, CO emitted from the surface is
407 first transported northward by maritime inflow associated with the summer monsoon before being
408 lifted to the free troposphere by deep convection and carried eastward by the strong westerlies.
409 Northward transport is most significant for CO from SC, for which emissions are from south of 30°N,
410 whereas outflow is confined to north of 35°N. Convection is expected to be stronger in summer than
411 in spring, resulting in more efficient lifting and subsequently, stronger outflow in the free troposphere.
412 In summer, the eastward fluxes of Chinese CO all take the common pathway confined to north of
413 35°N in the free troposphere, regardless of the latitudes from which emissions originated. In contrast,
414 outflow in springtime is strongest over the same latitudes of emissions. For example, outflow from SC
415 in springtime is strongest at 25°N, while that from NC is strongest at 40°N.

416 **6 Concluding Remarks**

417 The updated fine-resolution ($0.5^\circ \times 0.667^\circ$) nested-grid GEOS-Chem model developed here
418 allows for better representation of the heterogeneity in emissions and transport compared with the
419 coarse- and intermediate-resolution global models and the original nested-grid GEOS-Chem
420 model at $1^\circ \times 1^\circ$ resolution (Wang et al., 2004a). Boundary conditions for the fine-resolution
421 nested-grid model are provided by results from the coarse global model. Emissions over China in
422 the fine-resolution model show patterns of fossil fuel and biofuel combustion spatially

423 differentiated by economic development, industry structure, and population. The nested-grid
424 simulation suggests that the highest CO column density over East Asia in summertime is at the
425 Sichuan Basin, a feature not captured by the global model due to resolution limitations.
426 Influenced by the East Asian summer monsoon, the Sichuan Basin is a favorable location for
427 low-level stationary vortices (the southwest vortex) in summer that tend to trap pollutants over
428 the Basin, resulting in elevated levels of CO. By comparing surface CO simulated at different
429 model resolutions for the Beijing-Tianjin-Hebei city clusters, we found that the fine-resolution
430 nested-grid model is capable of resolving individual cities with high emission intensities. These
431 localized emissions would be smeared out over a coarse grid in the global models, leading to
432 underestimates of CO mixing ratio at suburban sites.

433 The nested-grid model was used to analyze the day-to-day variations in CO at a suburban site
434 near Beijing in summertime. The model was found to reproduce well the observed variations in
435 temperature and surface pressure but was found to overestimate wind speeds. Since the suburban
436 site is under the strong influence of Beijing urban emissions, overestimates in wind speeds by the
437 model result in more rapid dilution and greater export of local emissions out of the grid, leading
438 to underestimates of CO mixing ratios of the model. Tagged CO simulation results suggest that
439 regional emissions from Tianjin, Shandong, and Hebei make significant contributions to elevated
440 levels of CO over Beijing on polluted days. During these days, as much as 50% of CO in Beijing
441 was associated with emissions from the three regions. We found that the southeastward moving
442 cyclones that bring northwest winds to Beijing are the key meteorological mechanism

443 responsible for dispersion of pollution over Beijing in summer.

444 The overall fluxes of CO to the NW Pacific from Asia are found to decrease by a factor of
445 3-4 from spring to summer, consistent with the seasonality suggested by other studies (Liu et al.,
446 2004). Much of this reduction is driven by decreasing fluxes transported from India and
447 Southeast Asia in summer. CO originating in India and Southeast Asia accounts for about 60% of
448 the total fluxes in spring. The fluxes from East China are only 30% lower in summer than in
449 spring. Emissions from East China contribute about 40% of the total outflow of CO from Asia in
450 spring, increasing to 70-80% in summer. We found that the major export pathway for Asian CO is
451 in the EW direction in both spring and summer. Compared with springtime, summertime outflow
452 from all the tagged Chinese source regions is strongest at higher latitudes (north of 35°N). This
453 suggests that in summer, CO emitted from the surface is transported first northward by maritime
454 inflow associated with the summer monsoon before being lifted to the free troposphere by deep
455 convections and carried eastward by the strong westerlies. The export efficiency of CO is greater
456 in summer than in spring. The deeper convection in summer bringing CO to higher altitudes with
457 more efficient export is the important factor for higher export efficiency in summer. The analysis
458 suggests that despite the maritime inflow at lower latitudes in summer, summertime outflow of
459 CO from East Asia, which takes the pathway more north and toward higher altitudes, is important
460 for the global atmosphere.

Acknowledgement: The work of Kebin He and Dan Chen was supported by the National High Technology Research and Development Program of China (Grant No. 2006AA06A305) and China's National Basic Research Program (2005CB422201). Yuxuan Wang and Michael B. McElroy were supported by the National Science Foundation, Grant ATM-0635548. Dan Chen thanks the Harvard China Project for generously hosting her visit in 2007 and 2008, when the majority of her work was conducted. We thank Dr. David G. Streets and Dr. Qiang Zhang for providing the emission inventory data. We also thank Chris Nielsen, Jintai Lin, and Xi Lu for helpful discussions.

Reference

- An, J., Li, X., Wang, Y., Shi, L., Hu, F., and Xu, Y.: Measurements of Atmospheric Boundary Layer O₃, NO_x and CO in Summer with Beijing 325m Meteorological Tower, *Environmental Science*, 24(6), 43-47, 2003. [in Chinese]
- Bey, I., Jacob, D. J., Yantosca, R. M., Logan, J. A., Field, B., Fiore, A. M., Li, Q., Liu, H., Mickley, L. J., and Schultz, M.: Global modeling of tropospheric chemistry with assimilated meteorology: Model description and evaluation, *J. Geophys. Res.*, 106, 23,073–23,096, 2001.
- Cai, X., Zhang, R., Song, Yu., and Xie, S.: An Analysis on Background Concentration of PM₁₀ and SO₂ over Beijing Area, *Climatic and Environmental Research*, 9(3), 445-453, 2004. [in Chinese]
- Chang, C., Yia, L., and CHEN, G.: Numerical Simulation of Vortex Development during the 1992 East Asian Summer Monsoon Onset Using the Navy's Regional Model, *Monthly Weather Review*, 128(6), 1604-1631, 2000.
- DAO, Algorithm Theoretical Basis Document for Goddard Earth Observing System Data Assimilation System (GEOS DAS) with a focus on version 2, <http://dao.gsfc.nasa.gov/subpages/atbd.html>, 1996.
- Duncan, B., Martin, R., Staudt, A., Yevich, R., and Logan, J.: Interannual and Seasonal Variability of Biomass Burning Emissions Constrained by Satellite Observations, *J. Geophys. Res.*, 108(D2), 4040,

doi:10.1029/2002JD002378, 2003.

Fiore, A., Horowitz, L., Purves, D., Levy II, H., Evans, M., Wang, Y., Li, Q., and Yantosca, R.: Evaluating the contribution of changes in isoprene emissions to surface ozone trends over the eastern United States, *J. Geophys. Res.*, 110, D12303, doi:10.1029/2004JD005485, 2005.

Fuelberg, H., Kiley, C., Hannan, J., Westberg, D., Avery, M., and Newell, R.: Meteorological conditions and transport pathways during the Transport and Chemical Evolution over the Pacific (TRACE-P) experiment, *J. Geophys. Res.*, 108(D20), 8782, doi:10.1029/2002JD003092, 2003.

Jia, Y., Rahn, K., He, K., Wen, T., and Wang, Y.: A novel technique for quantifying the regional component of urban aerosol solely from its sawtooth cycles. *J. Geophys. Res.* 113, doi:10.1029/2008JD010389, 2008.

Koster, R., Suárez, M., Ducharne, A., Stieglitz, M., and Kumar, P.: A catchment-based approach to modeling land surface processes in a GCM, Part 1, Model Structure. *J. Geophys. Res.*, 105, 24809-24822, 2000.

Li, Q., Jacob, D., Park, R., Wang, Y., Heald, C., Hudman, R., Yantosca, R., Martin, R., and Evans, M.: North American pollution outflow and the trapping of convectively lifted pollution by upper-level anticyclone, *J. Geophys. Res.*, 110, D10301, 2005.

Liang, Q., Jaegle, L., Jaffe, D., Weiss-Penzias, P., Heckman, A., and Snow, J.: Long-range transport of Asian pollution to the northeast Pacific: Seasonal variations and transport pathways of carbon monoxide, *J. Geophys. Res.*, 109, D23S07, doi:10.1029/2003JD004402, 2004.

Liu, H., Jacob, D., Bey, I., Yantosca, R., Duncan, B., and Sachse, G.: Transport pathways for Asian pollution outflow over the Pacific: Interannual and seasonal variations, *J. Geophys. Res.*, 108, 8786, doi 10.1029/2002JD003102, 2003.

Park, R., Jacob, D., Kumar, N., and Yantosca R.: Regional visibility statistics in the United States: Natural and transboundary pollution influences, and implications for the Regional Haze Rule, *Atmos. Environ.*, 40(28), 5405-5423, 2006.

Rienecker, M., Suarez, M., Todling, R., Bacmeister, J., Takacs, L., Liu, H., Gu, W., Sienkiewicz, M., Koster, R., Gelaro, R., Stajner, I., and Nielsen, E.: The GEOS-5 Data Assimilation System -Documentation of Versions 5.0.1, 5.1.0, and 5.2.0, NASA/TM-2007-104606, Vol. 27. edited by Max J. Suarez.

Seinfeld, J., and Pandis S.: *Atmospheric Chemistry and Physics: From Air Pollution to Climate Change*, John Wiley, Hoboken, N. J. 1998.

Song, C., Byun, D., Pierce, R., Alsaadi, J., Schaack, T., and Vukovich, F.: Downscale linkage of global model output for regional chemical transport modeling: Method and general performance, *J. Geophys. Res.*, 113, D08308, doi:10.1029/2007JD008951, 2008.

Stieglitz, M., A. Ducharne, R.D. Koster, and M.J. Suarez,: The impact of detailed snow physics on the simulation of snow cover and subsurface thermodynamics at continental scales. *J. Hydromet.*, 2, 228-242. 2001.

Streets, D., et al.: An inventory of gaseous and primary aerosol emissions in Asia in the year 2000, *J. Geophys. Res.*, 108(D21), 8809, doi:10.1029/2002JD003093, 2003.

Streets, D., Zhang, Q., Wang, L., He, K., Hao, J., Wu, Y., Tang, Y., and Carmichael, G., Revisiting China's CO emissions after the Transport and Chemical Evolution over the Pacific (TRACE-P) mission: Synthesis of inventories, atmospheric modeling, and observations, *J. Geophys. Res.*, 111, D14306, doi:10.1029/2006JD007118, 2006

Sun, Y., Wang, Y., Liu, G., An, J., Ma, Z., Shi, L., and Xu, H.: Analysis for Vertical Profile of Atmospheric SO₂ During Air Seriously Polluted Days in Beijing, *Environmental Science*, 27(3), 408-414, 2006

Wang, Y., McElroy, M., Jacob, D., and Yantosca, R.: A nested grid formulation for chemical transport over Asia: Applications to CO, *J. Geophys. Res.*, 109, D22307, doi:10.1029/2004JD005237, 2004a.

Wang, Y., McElroy, M., Wang, T., and Palmer, P., Asian emissions of CO and NO_x: constraints from aircraft and Chinese station data, *J. Geophys. Res.*, 109, D24304, 2004b.

Xia, H., The Characteristics of Temperature inversion of the urban area in Beijing and its influence on the atmosphere pollution, *China Academic Journal Electronic Publishing House*, 6(2), 63-66, 2004. [in Chinese]

Yevich, R., and Logan, J.: An assessment of biofuel use and burning of agricultural waste in the developing world, *Global Biogeochem. Cycles*, 17 (4), 1095, doi:10.1029/2002GB001952, 2003.

You, C., Cai, X., Song, Y., and Guo, H., Local Atmospheric Circulations over Beijing-Tianjin Area in Summer, *Acta Scientiarum Naturalium Universitatis Pekinensis* , 42(6) , 779-783,2006. [in Chinese]

Zhang, Q., Streets, D. G., Carmichael, G., He, K., Huo, H., Kannari, A., Klimont, Z., Park, I., Reddy, S., Chen, D., Duan, L., Lei, Y., Wang, L. and Yao, Z.: Asian emissions in 2006 for the NASA INTEX-B mission, manuscript submitted to *Atmospheric Chemistry & Physics Discussions*, 2009.

Table 1. Average CO mixing ratios for Jul-Aug-Sep 2005 (unit: ppbv)

Suburban DL			Urban Beijing		
Observations	0.5° X 0.667° model	2° X 2.5° model	observations	0.5° X 0.667° model	2° X 2.5° model
802	710	486	1296	791	594

Table 2. Modeled percentage contributions of emissions from different tagged regions to CO levels at DL site (%)

Tagged Region	Jul	Aug	Sep	Summer Average
Beijing (BJ)	35.4	49.9	50.3	46.2
Tianjin-Hebei (TH)	20.0	15.8	16.8	17.3
Shandong & Hebei (SH)	9.9	1.8	3.4	4.5
Shanxi & Shaanxi (SX)	1.8	2.2	1.2	1.7
Northeastern China (NEC)	8.3	11.9	11.0	10.6
South China (SC)	3.3	0.7	0.3	1.2
All the other regions combined	22.4	18.8	18.4	19.6

Table 3. Export Efficiencies of CO for Tagged Regions

	Spring (MAM)			Summer (JJA)		
	E-W	N-S	Total	E-W	N-S	Total
NC (SH & TH & BJ)	0.36	0.09	0.45	0.48	0.18	0.66
SX	0.49	0.02	0.51	0.70	0.19	0.89
NEC	0.40	0.19	0.59	0.53	0.25	0.78
SC	0.58	0.07	0.65	0.75	0.13	0.88

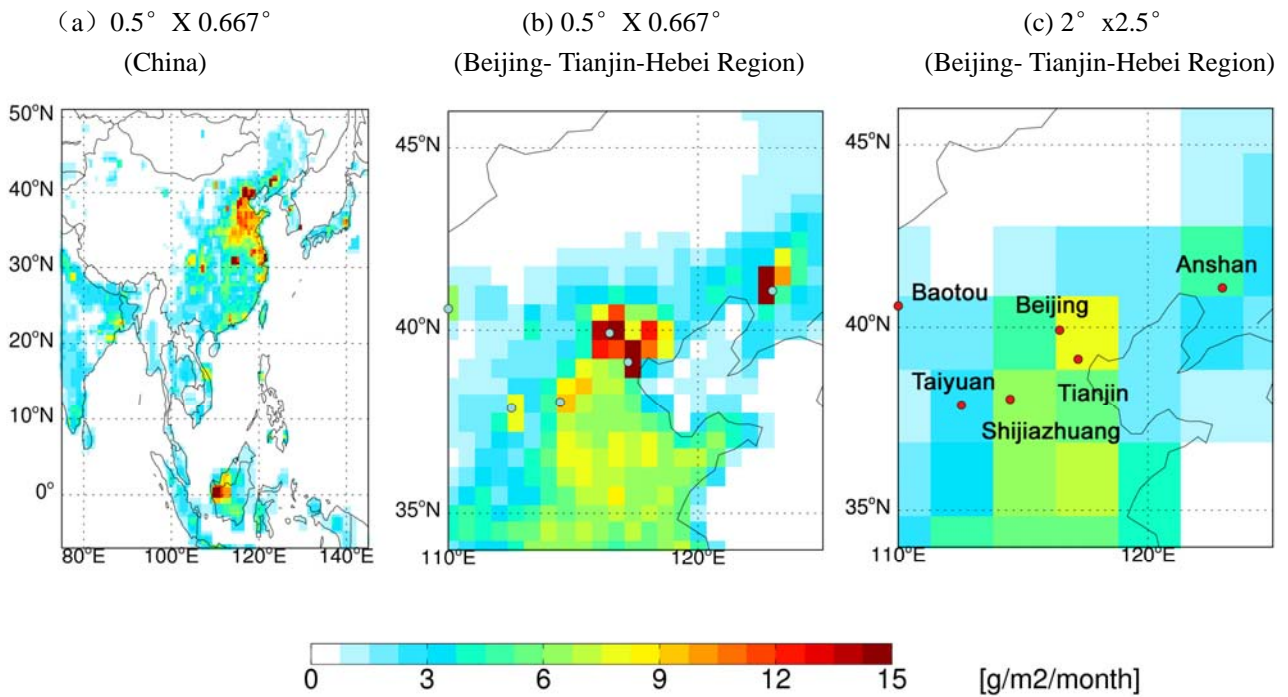


Fig. 1. (a)-(c) Total CO emissions for China and the Beijing- Tianjin-Hebei Region, (a) $0.5^\circ \times 0.667^\circ$ (China), (b) $0.5^\circ \times 0.667^\circ$ (Beijing- Tianjin-Hebei Region), (c) $2^\circ \times 2.5^\circ$ (Beijing- Tianjin-Hebei Region). Units are in $\text{g/m}^2/\text{month}$. Geophysical locations of capital cities in the region are illustrated in Fig. 1c.

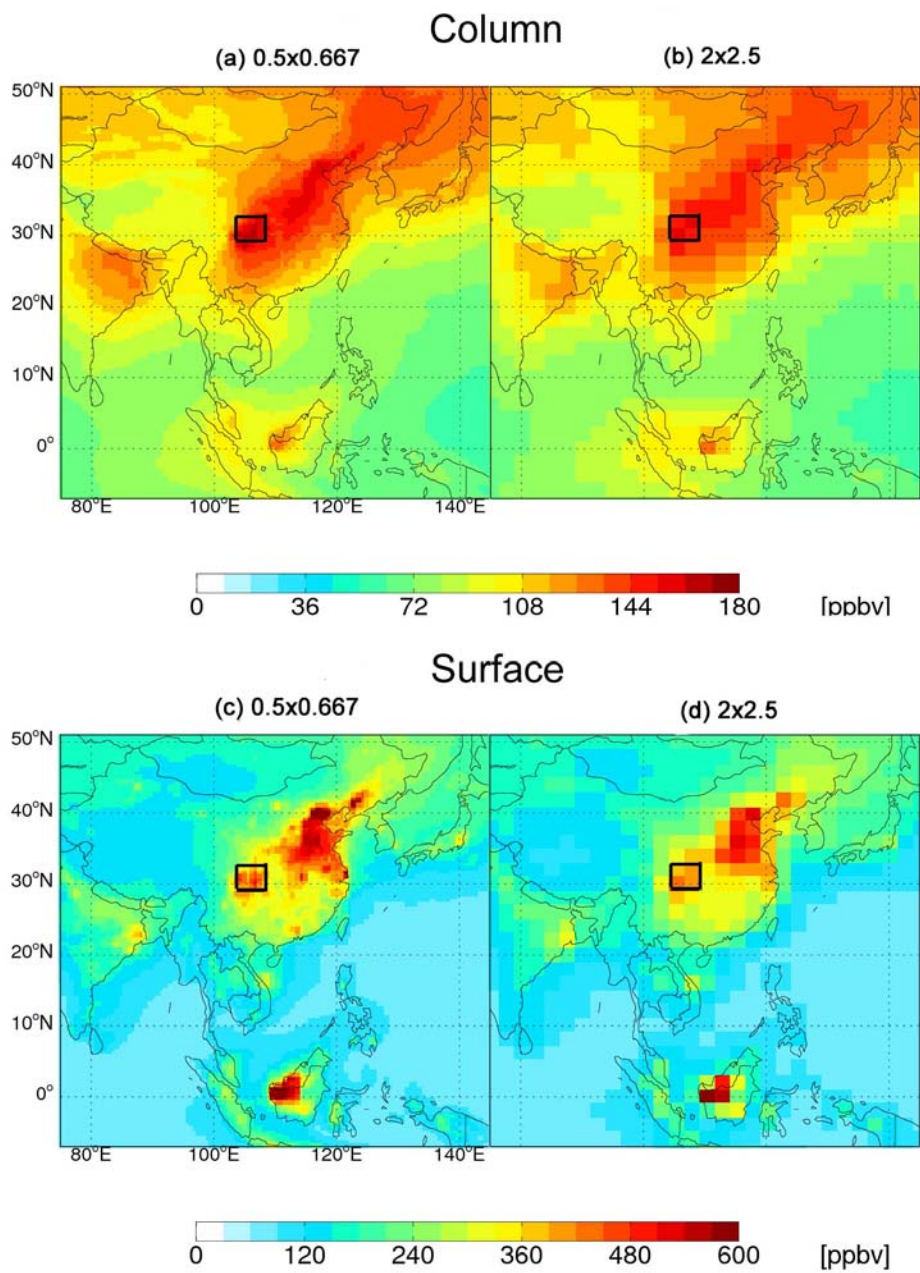


Fig. 2. Comparisons of CO mixing ratios averaged in the whole column (troposphere and stratosphere) and surface for August 2005, simulated by (a) the fine-resolution ($0.5^\circ \times 0.667^\circ$) regional simulation in column, (b) the intermediate-resolution ($2^\circ \times 2.5^\circ$) global simulation in column, (c) the fine-resolution ($0.5^\circ \times 0.667^\circ$) regional simulation at surface, and (d) the intermediate-resolution ($2^\circ \times 2.5^\circ$) global simulation at surface.

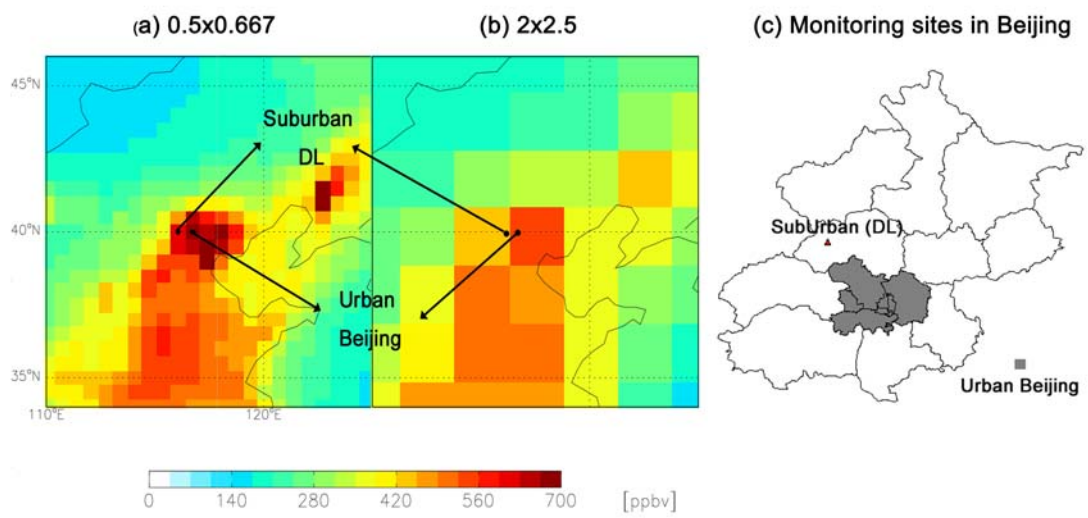
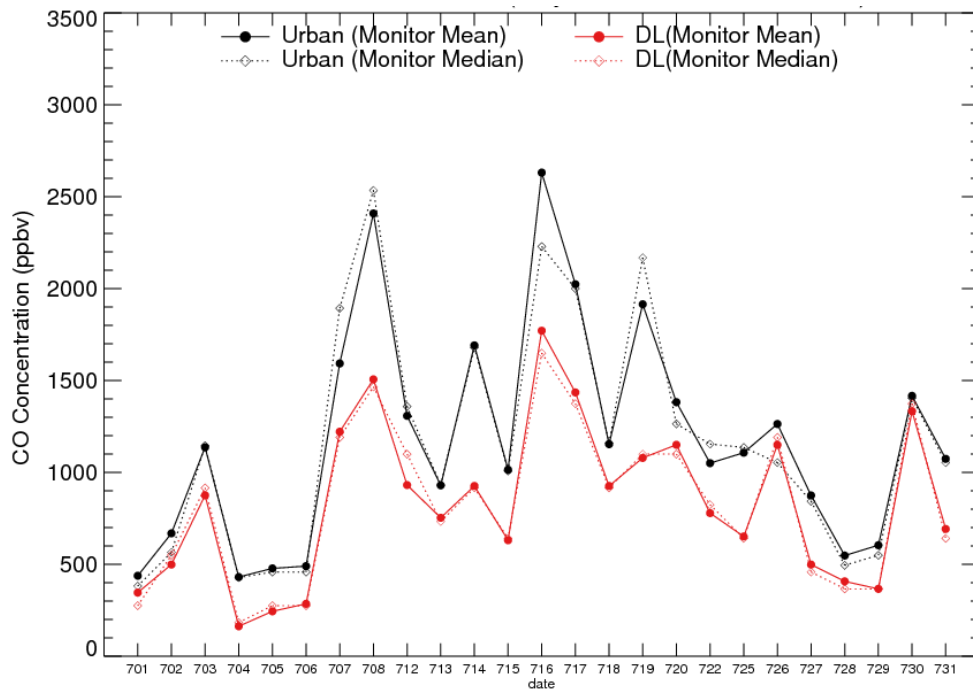
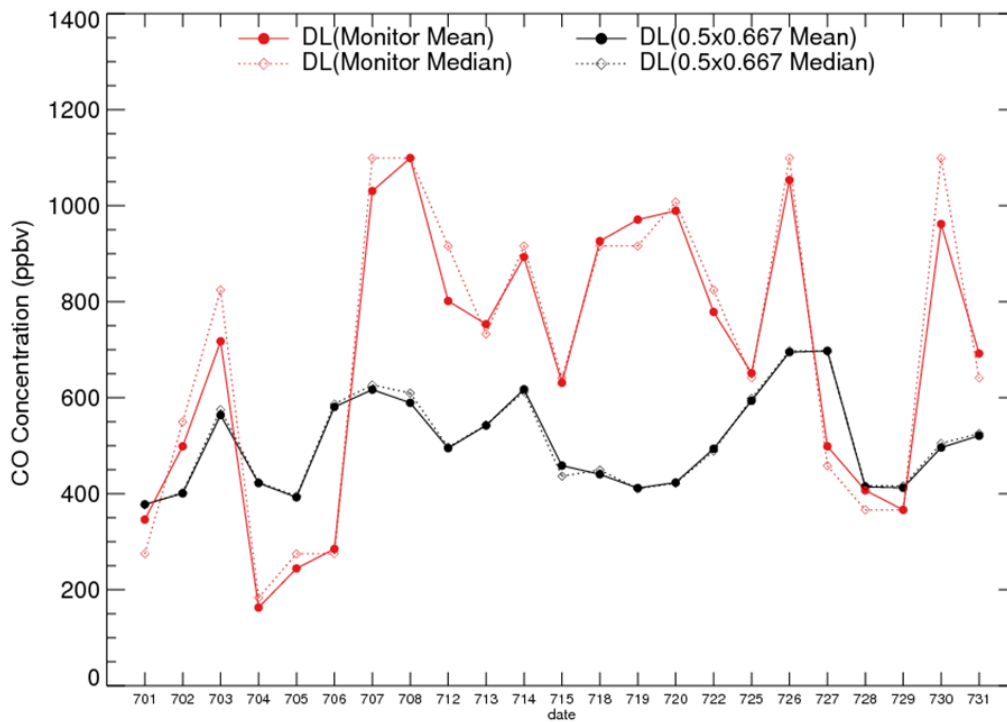


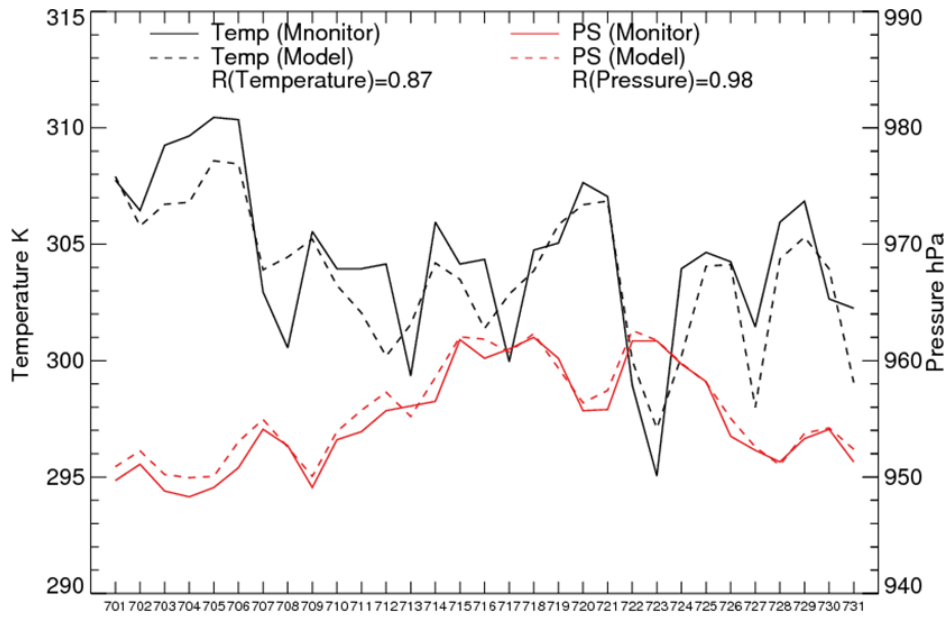
Fig. 3. Comparison of surface CO mixing ratio for the Beijing- Tianjin-Hebei Region for August 2005. (a) $0.5^{\circ} \times 0.667^{\circ}$. (b) $2^{\circ} \times 2.5^{\circ}$. Units are in ppbv. (c) Geophysical locations of monitoring sites in the region.



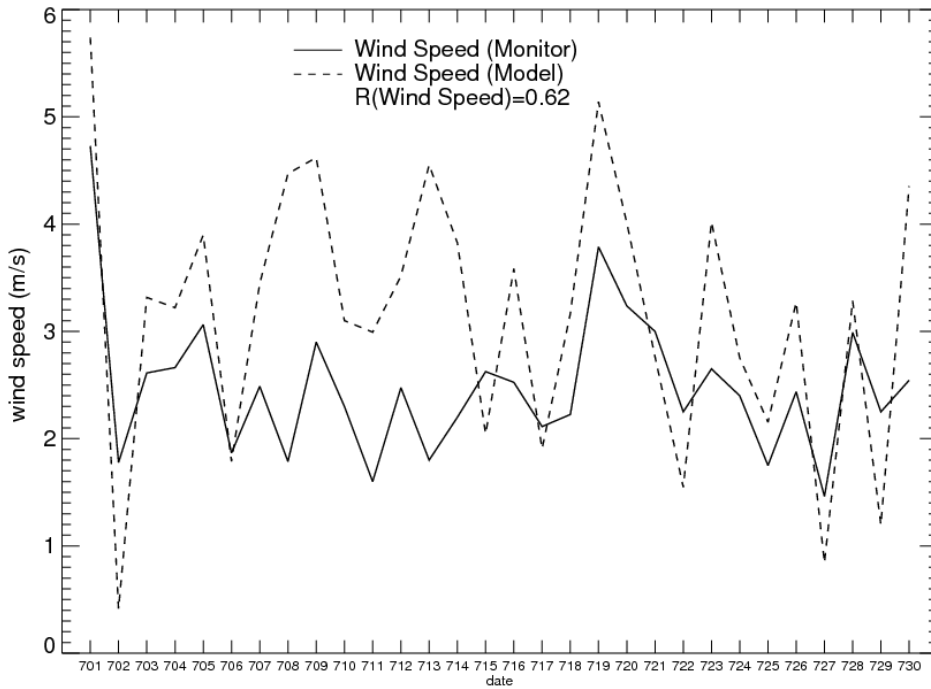
(a) Daily CO concentrations at urban and DL sites for July 2005.



(b) Daily CO concentration at DL sites for July 2005 (The hours where monitoring values are larger than 1300 ppbv are omitted both for monitoring and simulation results).



(c). Temperature and Pressure for 14:00 at DL sites for July, 2005.



(d). Wind speed for 14:00 at DL sites for July, 2005.

Fig. 4. Time series of CO concentration, wind speed, temperature, and pressure. Monitored and modeled in Beijing for July 2005.

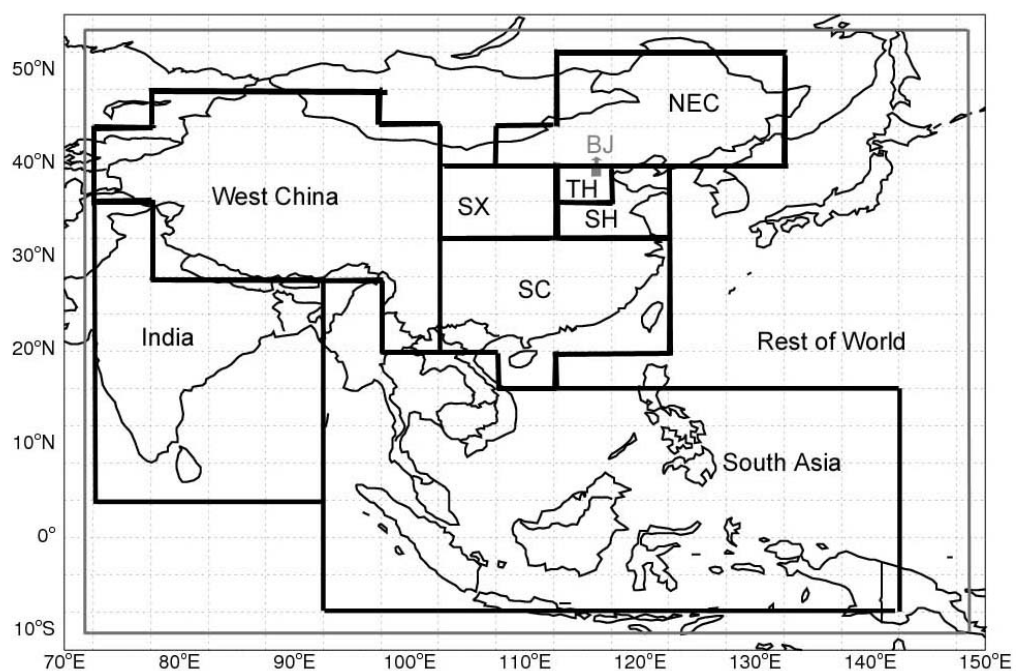


Fig. 5. Schematic representation of regional GEOS-Chem domains and source regions for tagged CO simulation. Regional domains are defined by the outermost thin gray lines, and the thick gray line is the actual boundary of the nested model. The grid boxes outside the gray rectangle in the fine-resolution domain define the buffer zone for boundary conditions.

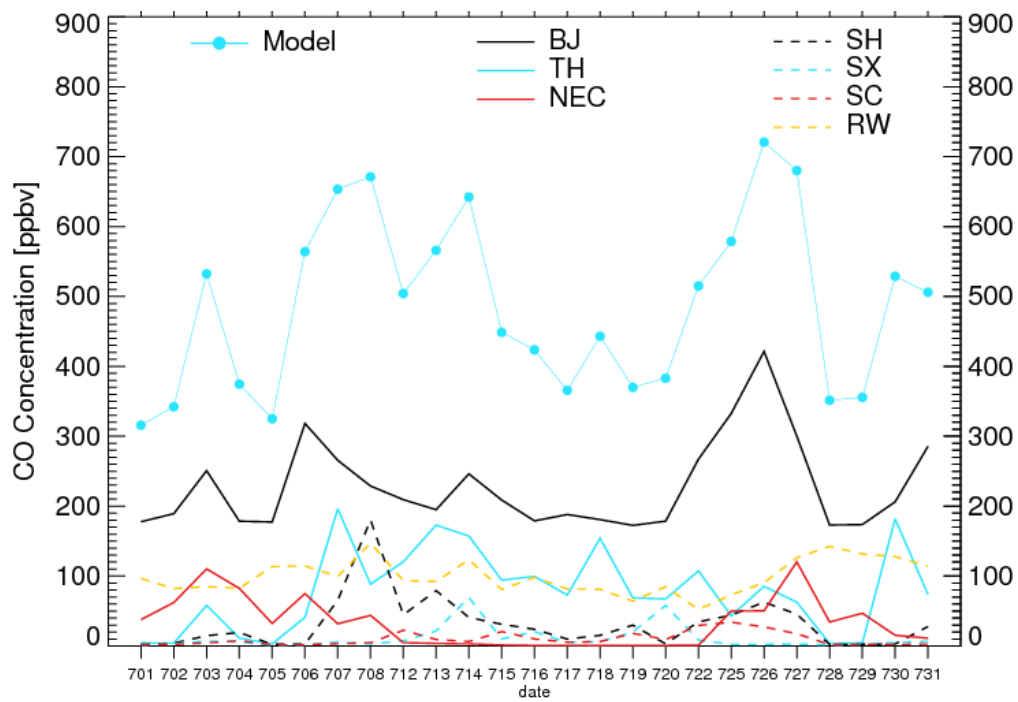


Fig. 6. Time series of daily contributions from tagged regions for July 2005 (unit: ppbv). (Blue solid line is the modeled total daily CO concentration at DL sites. Black, blue, and red solid lines are contributions from Beijing (BJ), Tianjin & Hebei (TH), and Northeastern China (NEC). The dashed lines are for the other tagged regions, Shandong and Hebei (SH, black dashed), Shanxi and Shaanxi (SX, blue dashed), South China (red dashed), and Rest of World (yellow dashed)).

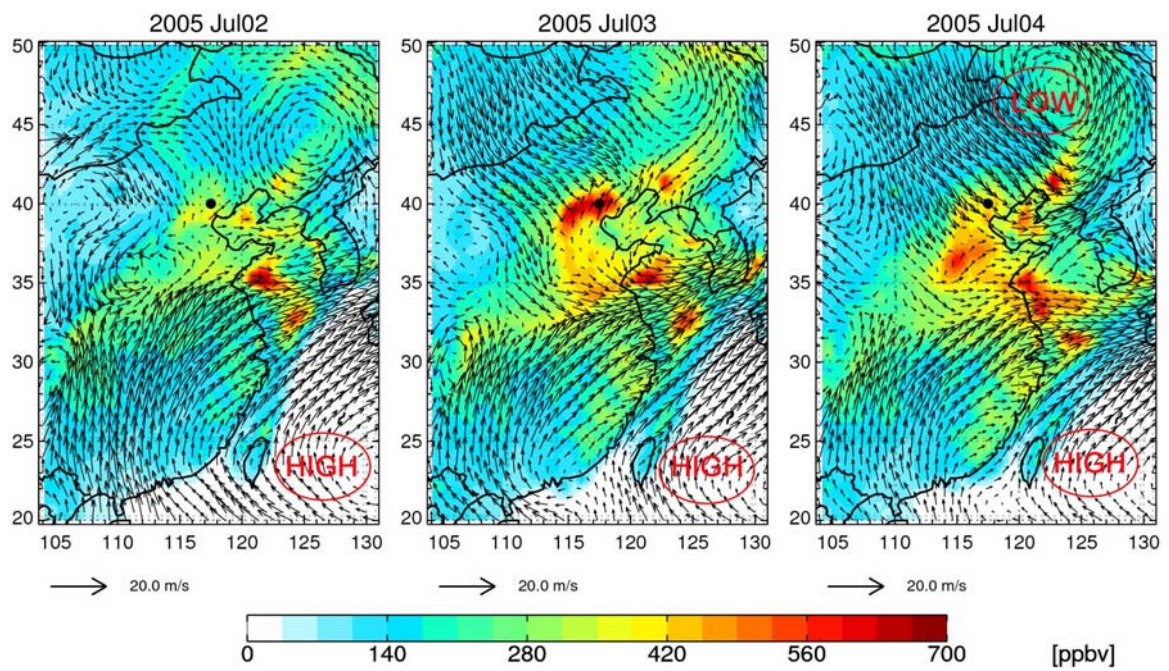


Fig. 7. Surface wind vectors and CO concentrations for the period of 2-4 July 2005.

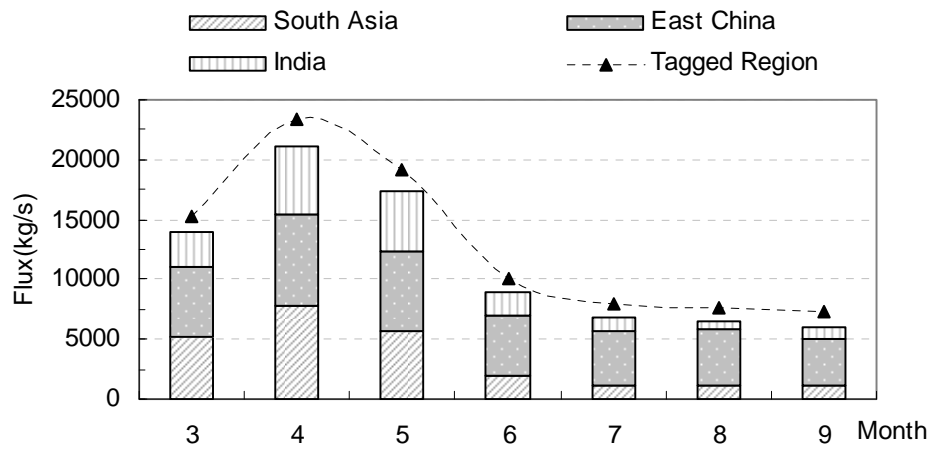


Fig. 8. Export fluxes of CO at 140° E contributed by emissions from different source regions. The domain adopted to evaluate the export fluxes is defined as 80°-140°E longitude, 10°-50°N latitude, and 0-12 km altitude. East China refers to the combination of SH, TH, BJ, SC, NEC, and SX. (c.f. Fig. 5).

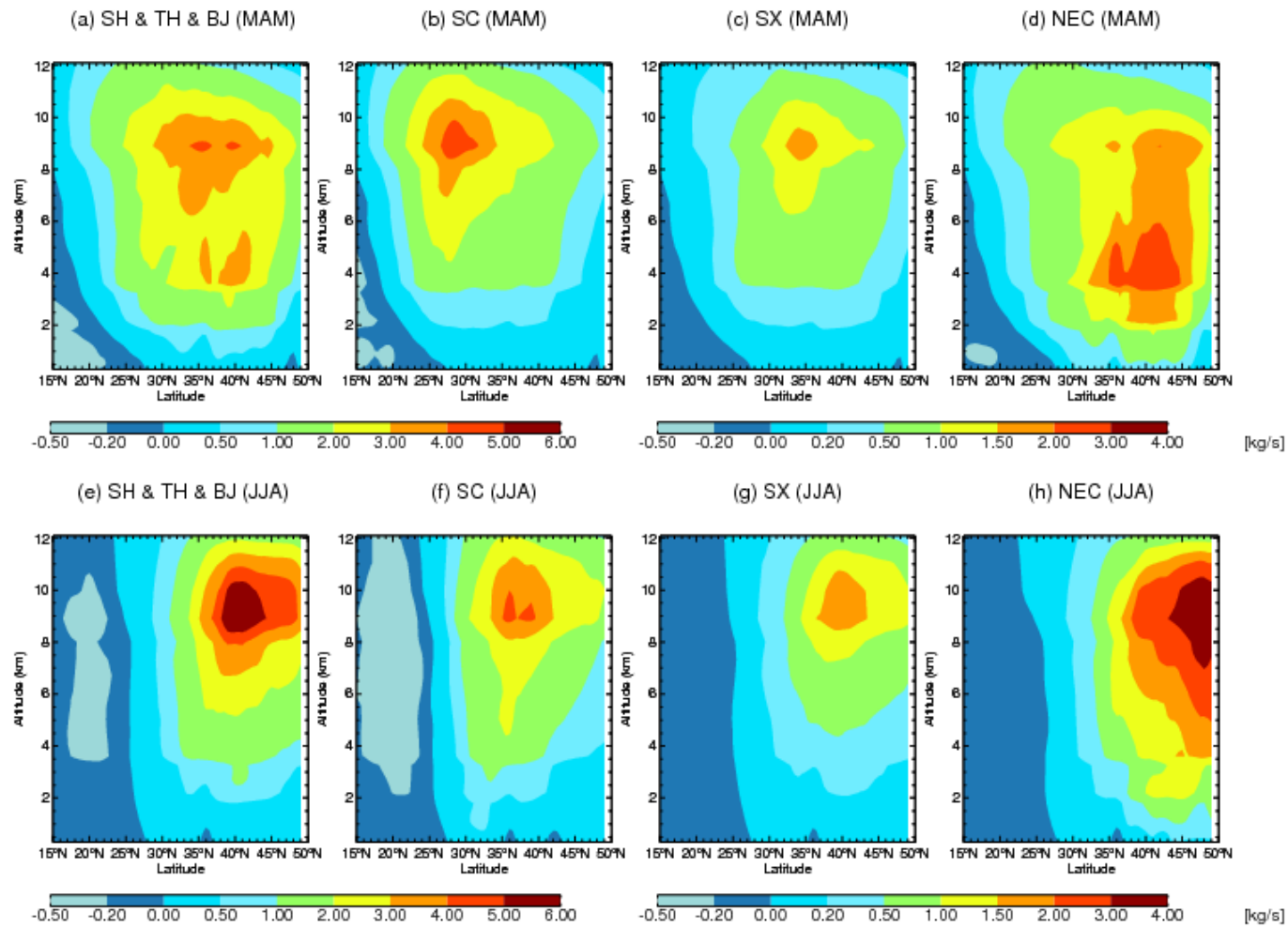


Fig. 9. Latitude-altitude cross sections at 140° E of seasonal mean fluxes of tagged CO tracers for spring (MAM) and summer (JJA) 2005.